Contents lists available at ScienceDirect

Transactions of Nonferrous Metals Society of China

36(2026) 355−370

www.tnmsc.cn

Effects of addition of Mn on microstructure, mechanical properties and corrosion behavior of T6-treated Al−Si−Mg alloys

Shan-liang XU [a], Hai-long JIA [a,b,*], Da-wei WANG [a], Min ZHA [a,b], Jia-wang SONG [a], Xiao-li ZHOU [a], Pin-kui MA [a,**]

[a] Key Laboratory of Automobile Materials of Ministry of Education, School of Materials Science and Engineering, Jilin University, Changchun 130025, China;

[b] International Center of Future Science, Jilin University, Changchun 130012, China

Abstract: The impact of Mn addition on the microstructure, mechanical properties and corrosion behavior of T6-treated Al−Si−Mg−xMn (x=0.2−1.0 wt.%) alloys in a 3.5 wt.% NaCl solution was investigated. The results showed that adding 0.2 wt.% Mn to T6-treated Al−Si−Mg alloys enhanced the corrosion resistance by promoting the formation of α-AlFeMnSi phase, characterized by smaller absolute Volta potential values compared to eutectic Si, β-AlFeSi and π-AlFeMgSi phases. However, the addition of 0.5 wt.% Mn and 1.0 wt.% Mn to the T6-treated Al−Si−Mg alloys increased the size of the α-AlFeMnSi phase. This decreased the properties of T6-treated Al−Si−Mg alloys. Therefore, the optimum Mn content was 0.2 wt.%, providing a novel approach for synergistically enhancing mechanical properties and corrosion resistance of Al−Si−Mg alloys.

Key words: Al−Si−Mg−xMn alloys; secondary phase; absolute Volta potential; microstructure; mechanical properties; corrosion resistance

1 Introduction

Al−Si alloys are widely used in the automotive and aerospace industries due to their remarkable combination of specific strength, excellent castability and mechanical properties [1−4]. However, these alloys, especially in the peak-aged state, are prone to localized corrosion [5,6]. Thus, enhancing the corrosion resistance is crucial for prolonging the service life of Al−Si alloys [7,8]. Many researchers have identified a strong correlation between the corrosion behavior of Al−Si alloys and secondary phases, in terms of the type, number density, distribution and volume fraction [9]. Although the presence of dispersed fine secondary phases improves strength, it generally degrades the corrosion resistance [10−12]. Therefore, controlling secondary phases remains a significant challenge when aiming to improve both mechanical and corrosion properties of Al−Si alloys.

In recent decades, a large number of studies have concentrated on tailoring secondary phases in Al−Si alloys. These efforts encompass alterations in casting and heat treatment parameters, as well as introduction of various elements. For example, the rheological casting of A356 alloy results in the formation of spherical α-Al phase, the refinement of Fe-rich phases and eutectic Si particles. The refined microstructures lead to the small Volta potential difference between secondary phases and α-Al matrix [13]. However, the Q phases ($Al_4Mg_8Si_7Cu_2$) that continuously distributed at grain boundaries work as cathodes, while adjacent precipitate-free

Corresponding author: *Hai-long JIA, Tel/Fax: +86-431-85095415, E-mail: jiahailong@jlu.edu.cn;
**Pin-kui MA, Tel/Fax: +86-431-85095415, E-mail: mapk@jlu.edu.cn

https://doi.org/10.1016/S1003-6326(25)66969-X

Received 4 April 2024; accepted 24 December 2024

zone acts as anodes, leading to the micro-galvanic corrosion of the over-aged Al−Mg−Si−Cu alloy [14]. Magnesium (Mg) and copper (Cu) can enhance the strength and hardness of Al alloys [15]. Nevertheless, it is crucial to note that Al_2Cu works as the cathode, while Mg_2Si serves as the anode relative to α-Al matrix. This interaction has the potential to expedite the corrosion process in Al−Si alloys [16,17]. For instance, the addition of 0.5 wt.% Ni to the Al−Si−Mg−Cu alloy promotes the formation of γ-Al_7Cu_4Ni phases. The γ-Al_7Cu_4Ni phases act as the primary cathodes, intensifying localized pitting and, consequently, reducing the overall corrosion resistance [18]. Similarly, introducing 0.5 wt.% Mn and 1.0 wt.% Cu into the Al−Si−Mg alloy promotes the formation of Cu-rich *Q* phases and Mn-rich phases. These phases lead to the anodic dissolution of adjacent Al, resulting in localized pitting corrosion [19]. In contrast, the addition of 0.9 wt.% Yb to ADC12 alloy induces the Al_3Yb phase on Si phase. This modification effectively restrains the growth of Si phases and mitigates corrosion activity within the cathode regions [20]. The introduction of La in Al−Mg−Si alloys results in discrete short rod-like Si particles and Mg_2Si particles with a La-rich surface shell, which retards the dissolution of Mg_2Si particles [21]. The improved corrosion resistance of Al−Mg−Si alloys with 0.5 wt.% TiC_p can be attributed to the reduction of Mg_2Si and excessive Si phases at grain boundaries after aging, leading to a decreased corrosion rate [22]. Nevertheless, the industrial applications of rare earth element and nano-sized ceramic particles are restricted due to their high costs and complex preparation processes.

In this study, we systematically analyzed microstructure, mechanical properties and the corrosion behavior of T6-treated Al−Si−Mg−*x*Mn alloys. The corrosion resistance was assessed by a combination of immersion testing and electrochemical experiments. Furthermore, the micro-galvanic corrosion behavior of secondary phases in T6-treated Al−Si−Mg−*x*Mn alloys was investigated through scanning Kelvin probe force microscope (SKPFM). The methodology and findings of this work provide a theoretical basis for the development of Al−Si alloys with excellent corrosion resistance and mechanical properties.

2 Experimental

2.1 Materials preparation

Four alloys, i.e., Al−Si−Mg (Base), Al−Si−Mg−0.2Mn (Base-0.2Mn), Al−Si−Mg−0.5Mn (Base-0.5Mn) and Al−Si−Mg−1.0Mn (Base-1.0Mn) alloys were fabricated using pure Al (99.90 wt.%), pure Mg (99.99 wt.%), Al−20wt.%Si, and Al−10wt.%Mn master alloys in an electric resistance furnace. The measured chemical compositions of these alloys are given in Table 1. The casting process involves the following steps: firstly, pure Al, Al−20wt.%Si and Al−10wt.%Mn master alloys were melted at 750 ℃. Subsequently, pure Mg wrapped with an Al foil was introduced into the melt at 720 ℃, followed by stirring. The melt was then stirred with high-purity Ar for 3 min and finally poured into a steel mold, which was preheated to 250 °C. Samples with dimensions of 120 mm × 20mm × 1.5 mm were cut from as-cast ingots for the subsequent T6 heat treatment, involving a solution treatment at 535 °C for 5 h, followed by aging at 180 °C for 5 h.

Table 1 Measured chemical compositions of four studied alloys (wt.%)

Sample	Si	Mg	Mn	Fe	Al
Base	7.2	0.46	0	0.13	Bal.
Base-0.2Mn	7.1	0.45	0.21	0.12	Bal.
Base-0.5Mn	7.2	0.43	0.47	0.14	Bal.
Base-1.0Mn	7.1	0.42	0.98	0.13	Bal.

2.2 Immersion and electrochemical tests

The sample surfaces for immersion and electrochemical tests were initially ground using SiC papers and subsequently mechanically polished using diamond pastes. Electrochemical tests were carried out using a Princeton Versa-STAT3F electrochemical workstation. Samples (10 mm × 10 mm × 1.5 mm) were sealed with epoxy for both immersion and electrochemical tests. For electrochemical tests, a standard three-electrode system was used, consisting of test alloys having an exposed area of 1 cm^2 as the working electrode, a platinum plate as the counter electrode and a saturated calomel electrode (SCE) as the reference electrode. The open circuit potential (OCP) was recorded for 1800 s to establish a stable state before conducting the polarization tests. Potentiodynamic

polarization tests were initiated from −1.2 to 0.1 V at a scanning rate of 1 mV/s. Electrochemical impedance spectroscopy (EIS) measurements were taken after varying immersion periods (3 and 5 d). The frequency range of electrochemical impedance spectroscopy (EIS) ranged from 100 kHz to 10 mHz. The amplitude of the sinusoidal potential signal was 5 mV. The EIS data were fitted using the Zsimpwin software. To guarantee reproducibility, each electrochemical measurement was carried out three times.

2.3 Microstructure characterization

Microstructures were analyzed using scanning electron microscopy (FE-SEM, Zeiss Sigma 500, Germany) equipped with energy-dispersive spectroscopy (EDS, Oxford INCA-X-Max). BSE and EDS samples were prepared through mechanical grinding and polishing. Phase compositions were determined using X-ray diffraction (XRD, D/Max 2500PC Rigaku) with Cu K_α radiation in the 2θ range of 20°−80° and a scanning rate of 2 (°)/min. The 3D corrosion morphology was assessed using laser scanning confocal microscopy (LSCM, OLS3000). Scanning Kelvin probe force microscope (SKPFM) measurements were carried out using a Dimension Icon instrument with a NanoScopeV9 controller (Bruker, Inc). An FEI Tecnai F30 transmission electron microscope (TEM) was employed to identify nanoscale particles in T6-treated alloys. Additionally, tensile tests were conducted on bone-shaped samples with a gauge length of 30 mm at room temperature, and the strain rate was 1×10^{-3} s^{-1}.

3 Results

3.1 Microstructures of T6-treated alloys

Figure 1 displays the phase content−temperature composition diagrams of the four studied alloys, aiming to explore the impact of Mn contents on the formation of Fe-rich phases. In Fig. 1(a), the Base alloy contains β-AlFeSi, Mg_2Si, π-AlFeMgSi, and Si phases. When 0.2−1.0wt.%Mn is added, the β-AlFeSi and π-AlFeMgSi phases decrease in quantity, while the α-AlFeMnSi phase appears (as depicted in Figs. 1(b−d)). As a result, the calculated

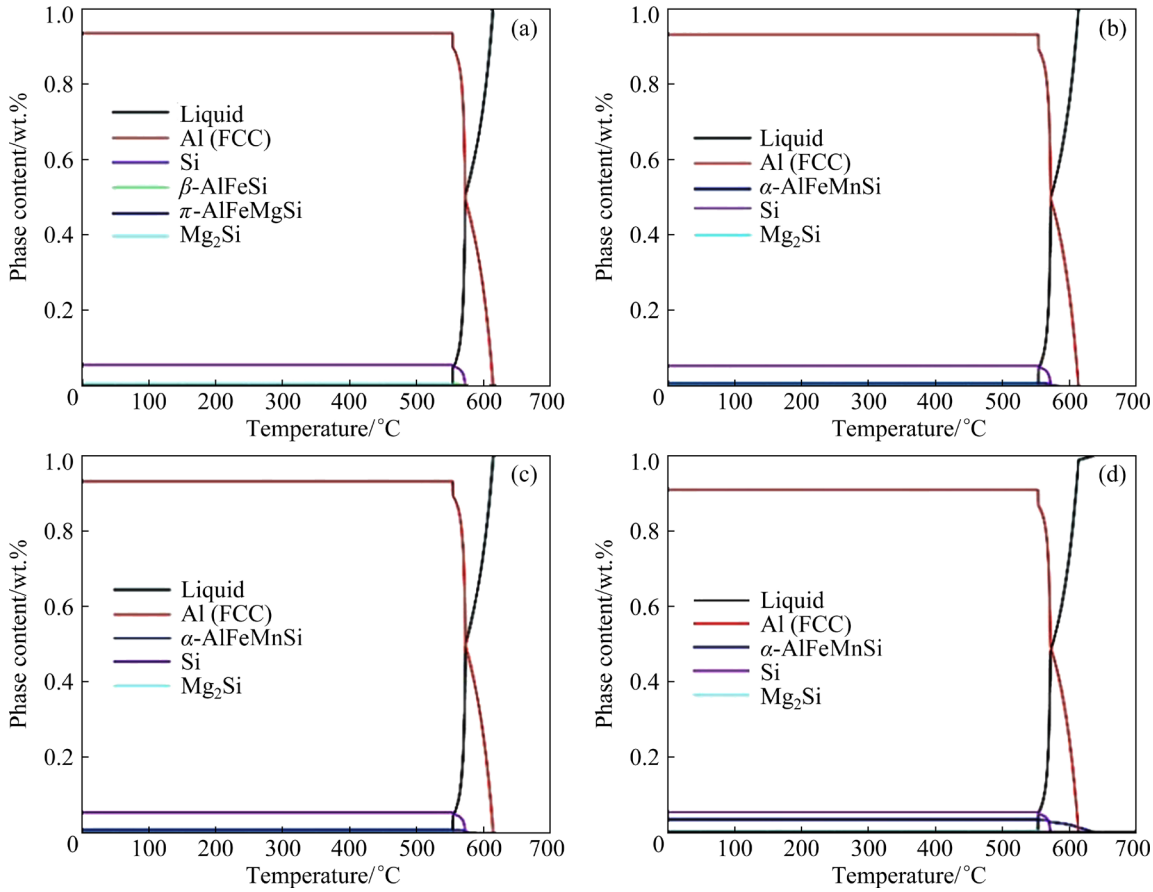

Fig. 1 Calculated phase content−temperature diagrams of four Al−Si−Mg−*x*Mn alloys: (a) Base; (b) Base-0.2Mn; (c) Base-0.5Mn; (d) Base-1.0Mn

phase composition−temperature diagrams imply that the addition of 0.2 wt.% Mn could potentially eliminate the π-AlFeMgSi and β-AlFeSi phases. Furthermore, the formation of the α-AlFeMnSi phase takes place prior to that of α-Al during the solidification process, indicating that Mn atoms have a tendency to bind with Fe atoms.

Figure 2 shows XRD patterns of the four T6-treated Al−Si−Mg−xMn alloys. It can be seen that the Base alloy is composed of α-Al, eutectic Si, β-AlFeSi, and π-AlFeMgSi phases (Fig. 1(a)). When 0.2−1.0 wt.% Mn is added to the Al−Si−Mg alloys, diffraction peaks corresponding to the α-AlFeMnSi phase emerge. This suggests that the β-AlFeSi and π-AlFeMgSi phases are transformed into the α-AlFeMnSi phase, which has also been reported in the relevant references [23,24].

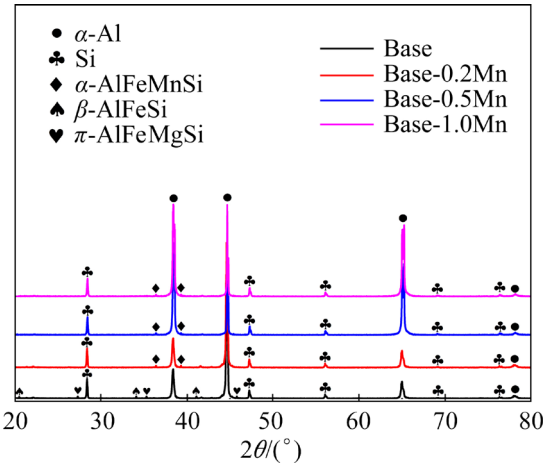

Fig. 2 XRD patterns of four T6-treated Al−Si−Mg−xMn alloys

Figure 3 illustrates BSE images and elemental distribution of the four T6-treated Al−Si−Mg−xMn alloys. In the Base alloy (Fig. 3(a)), needle-like β-AlFeSi and spherical π-AlFeMgSi phases are observed. As shown in Fig. 3(b), the addition of 0.2 wt.% Mn leads to a transformation of Fe-rich phases in Base alloy, converting the β-AlFeSi and π-AlFeMgSi phases into spherical α-AlFeMnSi phase. As the Mn content increases to 0.5 wt.% and then to 1.0 wt.%, the α-AlFeMnSi phase undergoes coarsening and transfers from a spherical shape to a needle-like morphology. Simultaneously, the eutectic Si phase is distributed on both sides of the needle-like α-AlFeMnSi phase (Figs. 3(c, d)). Nevertheless, when the Mn content exceeds 0.5 wt.%, the coarsening of α-AlFeMnSi phase becomes less pronounced, while the volume fraction increases significantly.

Figures 4(a−c) show representative TEM images of three T6-treated Al−Si−Mg alloys. Figures 4(d−g) depict HRTEM micrographs and their corresponding FFT patterns for the needle-like and granular β'' precipitates in T6-treated Base, Base-0.2Mn and Base-1.0Mn alloys [25,26]. Figure 5 shows the size distribution and number density of nano-scale needle-like and granular β'' precipitates. It seems that the Mn content does not have a significant effect on the size distribution and number density of nano-scale needle-like and granular β'' phases.

3.2 Mechanical properties

Figure 6(a) represents tensile engineering stress−strain curves for the four T6-treated Al−Si−Mg−xMn alloys, with corresponding tensile properties summarized in Table 2. It can be seen that the Base alloy has an ultimate tensile strength of ~333 MPa, a yield strength of ~292 MPa, and an elongation of ~4.3%. The ultimate tensile strength (~355 MPa) and elongation (~8.2%) of the T6-treated Base-0.2Mn alloy are significantly improved due to the presence of small-sized spherical α-AlFeMnSi phase [27]. Adding 0.5 wt.% Mn substantially reduces the elongation of the T6-treated Base-0.5Mn alloy, which is mainly due to the increased amount of needle-like α-AlFeMnSi phase [28,29]. The ultimate tensile strength and elongation of T6-treated Base-1.0Mn alloy are further decreased due to the increased quantity of needle-like α-AlFeMnSi phase. The needle-like α-AlFeMnSi phase serves as sources of cracks, reducing the ductility. Figure 6(b) compares the elongation and ultimate tensile strength of the T6-treated Al−Si−Mg, Al−Si−Mg−Re, Al−Si−Mg−Cu(Zn), and Al−Si−Mg−nanoparticle alloys reported in literature [30−37]. Al−Si−Mg alloys, when incorporated with additives such as Ce [30], Yb [31], Ti [32], Sc [33], Zn [34], Cu [35], and nanoparticles [36,37], commonly display high strength. However, this is invariably accompanied by a reduction in ductility. The T6-treated Base-0.2Mn alloy in this study presents a favorable combination of strength and ductility. This is mainly because the addition of Mn leads to the refinement and the morphology modification of the Fe-rich phases in the Al−Si−Mg alloys.

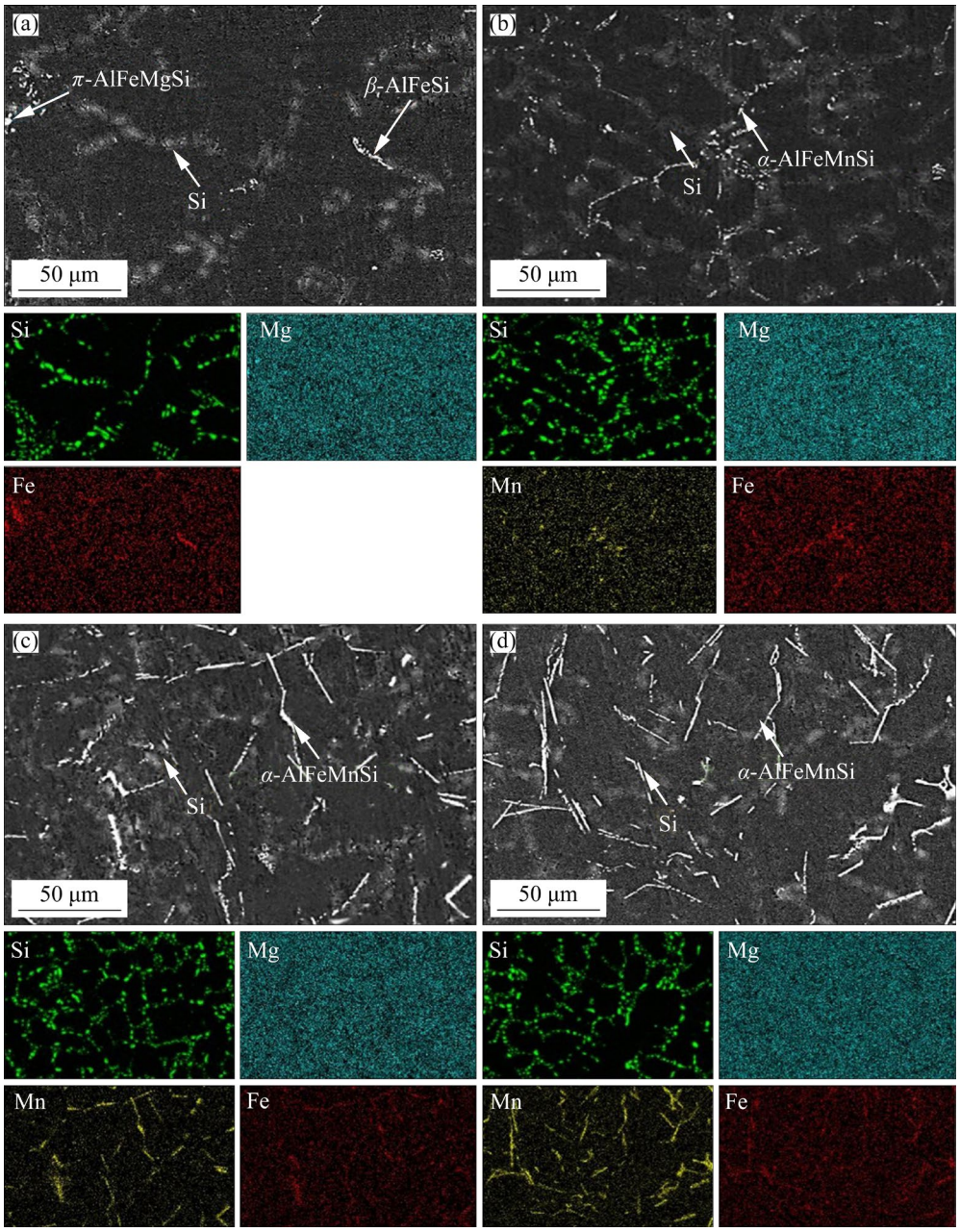

Fig. 3 BSE images and EDS maps of four T6-treated Al−Si−Mg−*x*Mn alloys: (a) Base; (b) Base-0.2Mn; (c) Base-0.5Mn; (d) Base-1.0Mn

3.3 Electrochemical characteristics

Immersion tests were conducted to assess the influence of Mn on the electrochemical behavior of the four T6-treated Al−Si−Mg−*x*Mn alloys, and the measurement included EIS and equivalent electrical circuit (EEC) fitting. EIS studies were carried out over various exposure time in 3.5 wt.% NaCl solution (Figs. 7(a−f)). Nyquist plots reveal two constants of time corresponding to capacitive loops at high frequencies (HFs) and low frequencies (LFs), associated with electrochemical responses of the passive films and localized corrosion process (Al−Al^{3+} process), respectively [12,21,38]. It has been indicated that the larger capacitive loop diameter implies a better corrosion resistance [39]. With increasing the immersion time, all alloys display similar electrochemical responses, while the diameter of capacitive loop decreases due to the infiltration of aggressive ions (Figs. 7(a, b)). Furthermore, Nyquist plots indicate that the corrosion resistance of T6-treated Al−Si−Mg alloy increases with the addition of 0.2 wt.% Mn but decreases with further addition of 0.5−1.0 wt.% Mn.

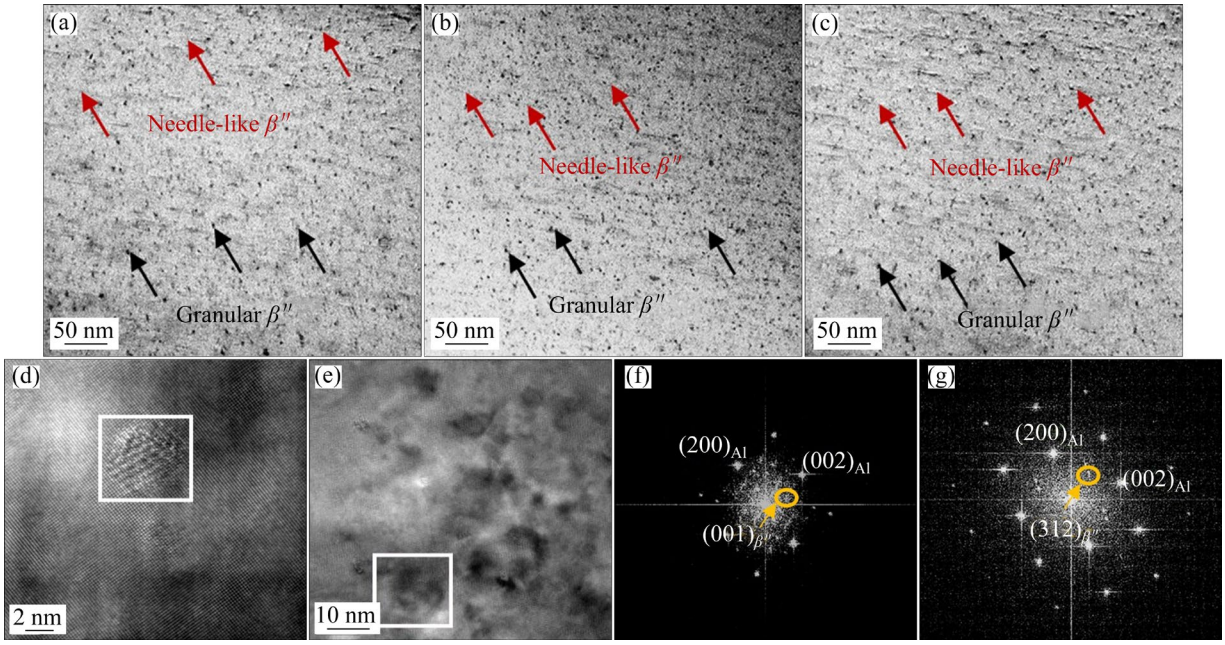

Fig. 4 TEM images showing needle-like and granular β'' precipitates in three T6-treated Al−Si−Mg−xMn alloys: (a) Base; (b) Base-0.2Mn; (c) Base-1.0Mn; (d, f) HRTEM image with corresponding FFT pattern for granular β'' precipitates; (e, g) HRTEM image with corresponding FFT pattern for needle-like β'' precipitates

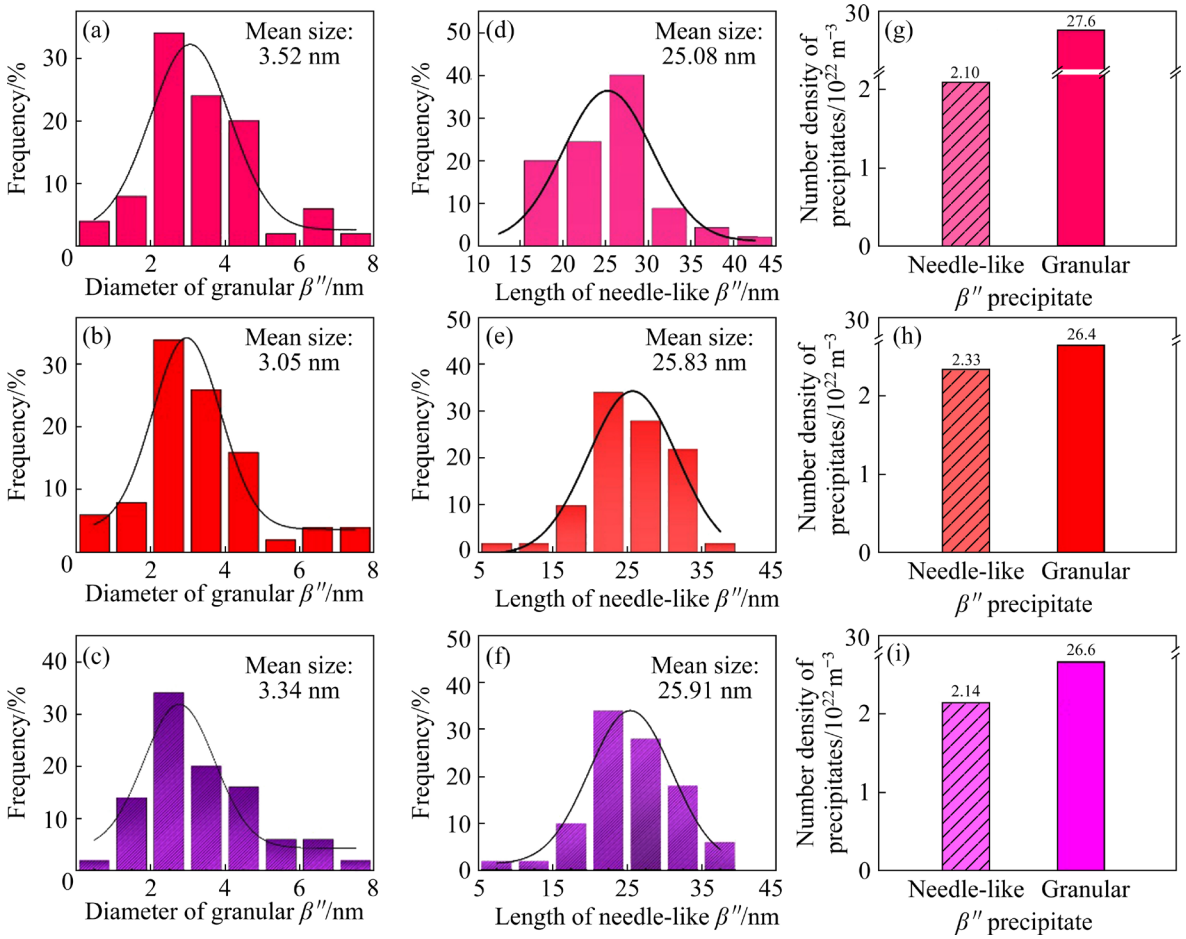

Fig. 5 Size distribution (a−f) and number density (g−i) of granular (a−c) and needle-like (d−f) β'' precipitates in three T6-treated Al−Si−Mg−xMn alloys: (a, d, g) Base; (d, e, h) Base-0.2Mn; (c, f, i) Base-1.0Mn

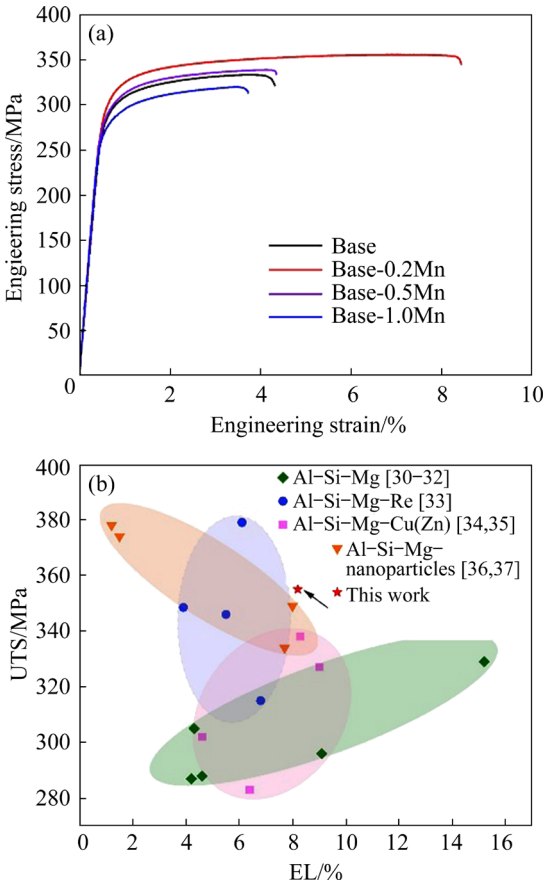

Fig. 6 (a) Tensile engineering stress−strain curves of four T6-treated Al−Si−Mg−*x*Mn alloys; (b) Comparison of elongation (EL) and ultimate tensile strength (UTS) of T6-treated Al−Si−Mg, Al−Si−Mg−Re, Al−Si−Mg−Cu(Zn) and Al−Si−Mg−nanoparticle alloys reported in literature [30−37]

Table 2 Mechanical properties of four T6-treated Al−Si−Mg−*x*Mn alloys

Alloy	UTS/MPa	YS/MPa	EL/%
Base	$333^{+5.3}_{-4.2}$	$292^{+2.5}_{-5.3}$	$4.3^{+2.2}_{-1.1}$
Base-0.2Mn	$355^{+8.2}_{-5.6}$	$308^{+4.1}_{-6.2}$	$8.2^{+2.4}_{-3.4}$
Base-0.5Mn	$338^{+6.9}_{-6.8}$	$292^{+6.3}_{-3.5}$	$4.2^{+2.1}_{-1.4}$
Base-1.0Mn	$320^{+3.2}_{-4.7}$	$277^{+3.4}_{-24}$	$3.7^{+0.2}_{-0.5}$

The Bode phase plots (Figs. 7(c, d)) suggest that the peak maxima decrease as the exposure duration increases, which confirms the decrease of capacitive behavior of the surface layer. The T6-treated Base-0.2Mn alloy exhibits the maximum peak value and peak width, indicating the highest corrosion resistance and lowest corrosion rate [40]. The Bode impedance magnitude plots indicate a reduction in impedance value ($|Z|$) within the low-frequency range as the exposure time increases (Figs. 7(e, f)). This is in line with the trend of the capacitive arc diameter (Figs. 7(a, b)). In the high-frequency region, the impedance value remains relatively low and constant, which is attributed to the solution resistance (R_s). Following a 5-day exposure, the low-frequency impedance increases until the Mn content reaches 0.2 wt.%, and then decreases with the addition of 0.5−1.0 wt.% Mn. This implies that the T6-treated Base-0.2Mn alloy exhibits greater stability in 3.5 wt.% NaCl solution compared to other three T6-treated alloys.

To gain a deeper understanding of the corrosion behavior, an equivalent electric circuit (EEC) to simulate the corrosion process is presented in Fig. 8. The EEC employed in this study comprises elements such as R_s, R_f (surface layer resistance), Q_1 (constant phase element of surface layer), R_{ct} (charge transfer resistance), and Q_2 (constant phase element of double layer). The parameters obtained through fitting are listed in Table 3. It can be seen that the R_f and R_{ct} values decrease with the increase of exposure time, which indicates that extending the immersion time in 3.5 wt.% NaCl solution will lead to a decline in corrosion resistance. After being exposed in 3.5 wt.% NaCl solution for 5 d, the R_f value of the T6-treated Base-0.2Mn alloy (12340 Ω·cm^2) is greater than that of the T6-treated Base alloy (7194 Ω·cm^2). However, further addition of Mn will lead to a decrease in the R_f value. Specifically, the R_f values of the T6-treated Base-0.5Mn alloy and the T6-treated Base-1.0Mn alloy are 11940 and 10220 Ω·cm^2, respectively. A higher R_f value indicates more stable passive films on the surface of the alloy [41]. This suggests that the passive films have formed on the surface and the T6-treated Base-0.2Mn alloy exhibits greater stability compared to its counterparts. Furthermore, the trend in the charge transfer resistance R_{ct} value aligns with that of the R_f value. The T6-treated Base-0.2Mn alloy exhibits the highest corrosion resistance, as evidenced by its higher R_{ct} and R_f values compared to other alloys. For various immersion test durations, the T6-treated Mn-added alloys exhibit significantly higher R_f and R_{ct} values compared to the T6-treated Mn-free alloy. This observation indicates that the T6-treated Mn-added alloys demonstrate superior corrosion resistance in the long immersion tests.

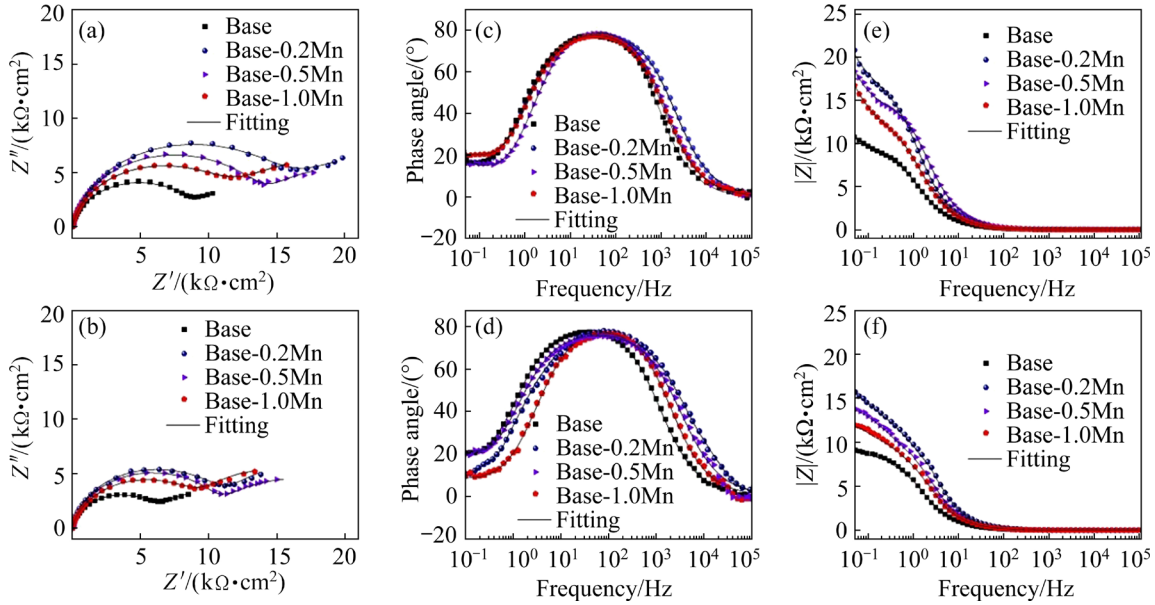

Fig. 7 EIS results of four T6-treated Al−Si−Mg−*x*Mn alloys immersed in 3.5 wt.% NaCl solution: Nyquist plots for 3 d (a) and 5 d (b); Bode phase plots for 3 d (c) and 5 d (d); Bode impedance magnitude plots for 3 d (e) and 5 d (f)

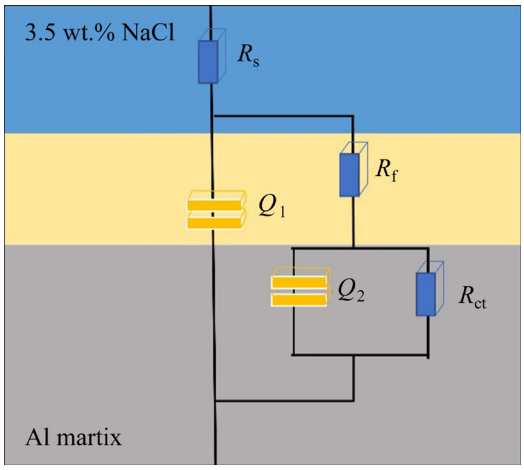

Fig. 8 Equivalent electrical circuit used to model experimental EIS data of four T6-treated Al−Si−Mg−*x*Mn alloys

3.4 Potentiodynamic polarization curves

Figure 9 displays the representative potentiodynamic polarization (PDP) curves for the four T6-treated Al−Si−Mg−*x*Mn alloys following a 5-day immersion in 3.5 wt.% NaCl solution. These curves exhibit two distinct stages, denoted as *AB* and *BC* (Fig. 9(a)). The *BC* branch corresponds to the anodic dissolution reaction stage, where the primary reaction involves the dissolution of *α*-Al matrix. In contrast, the *AB* branch represents the cathodic reaction stage, primarily characterized by oxygen absorption in 3.5 wt.% NaCl solution [5]. The pseudo-passivation tendency on the anodic branches can be attributed to partially protective passive films on the surface [42,43]. As the potential increases, a significant rise in corrosion current density is evident. This observation points to the deterioration of passive films and the rapid dissolution of anodic *α*-Al matrix. Beyond these breakdown potentials, the anodic kinetics of four alloys exhibits a similar trend. Furthermore, the polarization curves of the four alloys demonstrate similar cathodic kinetics, suggesting that the addition of Mn has a minimal impact on the cathodic kinetics of Al−Si−Mg alloys.

The determination of corrosion current density (J_{corr}) for the four T6-treated Al−Si−Mg−*x*Mn alloys is associated with the cathodic branch. Consequently, the corrosion current density has been determined using the method of extrapolating the cathodic Tafel region [44]. The calculated results in Table 4 reveal the corrosion potentials (φ_{corr}) for the four T6-treated alloys. It can be seen that the corrosion current density values of the four T6-treated alloys are in the following increasing order: Base-0.2Mn < Base-0.5Mn < Base-1.0Mn < Base. Typically, the corrosion current density is employed to assess corrosion rates [45]. Therefore, the T6-treated Base-0.2Mn alloy demonstrates superior corrosion resistance in 3.5 wt.% NaCl solution compared to other investigated alloys.

Table 3 Fitting parameters of EIS tests with exposure time of 3 and 5 d

Sample	Time/d	R_s/(Ω·cm^2)	Q_1/(Ω^{-1}·cm^{-2}·s^{n_1})	n_1	R_f/(Ω·cm^2)	Q_2/(Ω^{-1}·cm^{-2}·s^{n_2})	n_2	R_{ct}/(Ω·cm^2)
Base	3	8	2.33×10^{-5}	0.90	9846	1.33×10^{-3}	0.96	8221
	5	10	2.79×10^{-5}	0.90	7194	8.37×10^{-3}	0.94	6065
Base-0.2Mn	3	10	1.25×10^{-5}	0.91	17760	5.43×10^{-4}	0.87	12290
	5	9	1.71×10^{-5}	0.92	12340	6.03×10^{-4}	0.94	10800
Base-0.5Mn	3	9	8.34×10^{-6}	0.92	15780	4.50×10^{-4}	0.93	10200
	5	9	8.85×10^{-6}	0.90	11940	1.05×10^{-4}	0.89	8059
Base-1.0Mn	3	9	1.51×10^{-5}	0.90	13290	4.53×10^{-4}	0.97	11200
	5	9	1.77×10^{-5}	0.87	10220	4.16×10^{-4}	0.84	7846

n_1 and n_2 are the constant phase element (CPE) exponents for Q_1 and Q_2, quantifying the non-homogeneity of the electrode surface and the corrosion layer, respectively

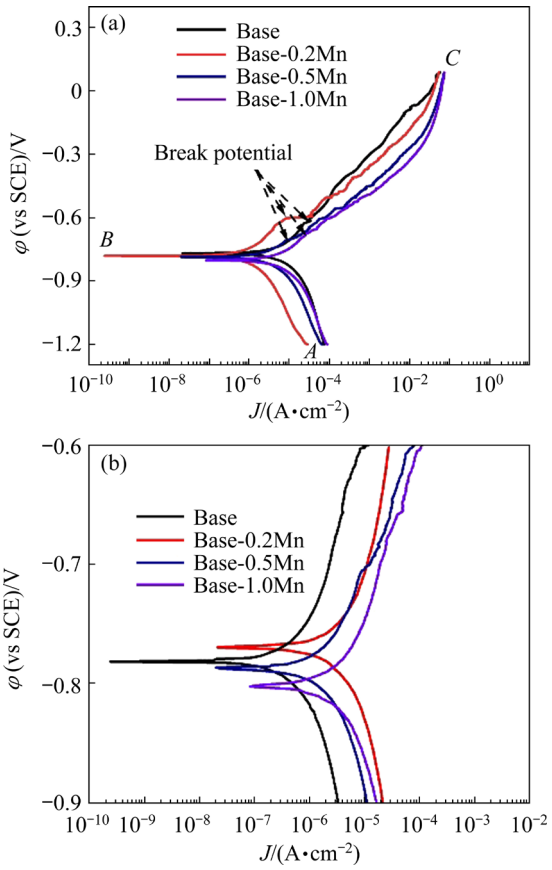

Fig. 9 (a) Potentiodynamic polarization curves of four T6-treated Al−Si−Mg−*x*Mn alloys after immersion in 3.5 wt.% NaCl solution for 5 d; (b) Enlarged potentiodynamic polarization spectra

Table 4 φ_{corr} and J_{corr} values extracted from potentiodynamic polarization in Fig. 9(a)

Alloy	φ_{corr}(vs SCE)/V	J_{corr}/(μA·cm^{-2})
Base	−0.775±0.033	6.79±1.310
Base-0.2Mn	−0.787±0.026	2.42±0.243
Base-0.5Mn	−0.797±0.032	2.79±0.351
Base-1.0Mn	−0.801±0.045	3.09±0.456

3.5 Corrosion morphologies

Figure 10 shows the BSE images illustrating microscopic morphologies of the four T6-treated Al−Si−Mg−*x*Mn alloys after immersion in 3.5 wt.% NaCl solution for 5 d without corrosion products. The eutectic Si phase possesses a higher absolute Volta potential value in comparison to the *α*-Al matrix and serves as the cathode, resulting in the formation of corrosion pits around the eutectic Si phase [41]. In the T6-treated Base alloy, small corrosion pits extend along the eutectic Si phase, ultimately leading to the formation of large corrosion pits (Fig. 10(a)). In the T6-treated Base-0.2Mn alloy, there is a decrease in the size of corrosion pits (Fig. 10(b)). However, in the T6-treated Base-0.5Mn and Base-1.0Mn alloys, the size of corrosion pits increases in comparison to that in the T6-treated Base-0.2Mn alloy (Figs. 10(c, d)), although it remains smaller than that of the T6-treated Base alloy. This phenomenon indicates that the formation of *α*-AlFeMnSi phase inhibits the formation and expansion of corrosion pits, resulting in a reduction in the size of corrosion pits in the T6-treated Al−Si−Mg−*x*Mn alloys.

Figure 11 illustrates LSCM images showing 3D macroscopic corrosion morphologies of the four T6-treated alloys after immersion in 3.5 wt.% NaCl solution for 18 d, without corrosion products. For the T6-treated Base alloy (Fig. 11(a)), some large corrosion pits are observed, indicating the presence of heterogeneous corrosion spreading across the surface and poor corrosion resistance. Upon the introduction of 0.2 wt.% Mn, the corroded surface becomes relatively flat and lacks prominent corrosion pits (Fig. 11(b)). This phenomenon suggests that the addition of 0.2 wt.% Mn substantially reduces

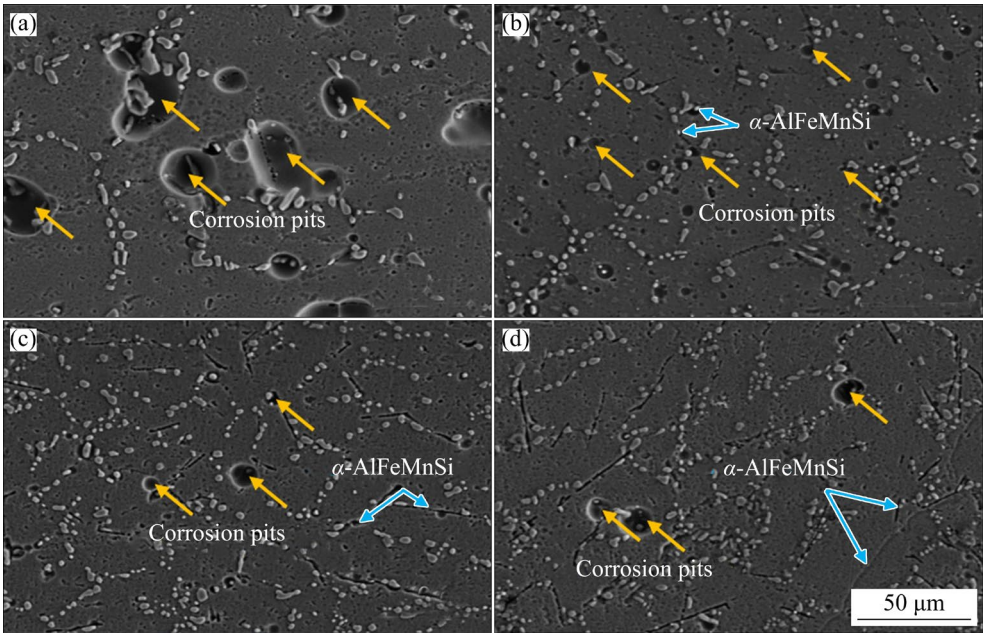

Fig. 10 BSE images showing corrosion morphologies of four T6-treated Al−Si−Mg−*x*Mn alloys after immersion in 3.5 wt.% NaCl solution for 5 d without corrosion products: (a) Base; (b) Base-0.2Mn; (c) Base-0.5Mn; (d) Base-1.0Mn

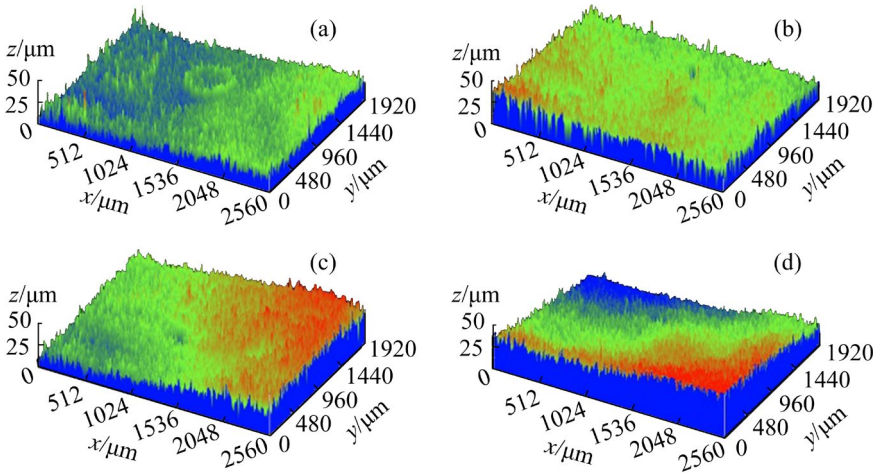

Fig. 11 LSCM images showing 3D corrosion morphologies of four T6-treated Al−Si−Mg−*x*Mn alloys after immersion in 3.5 wt.% NaCl solution for 18 d without corrosion products: (a) Base; (b) Base-0.2Mn; (c) Base-0.5Mn; (d) Base-1.0Mn

the localized corrosion in the T6-treated Base-0.2Mn alloy. However, many shallow corrosion pits appear in the T6-treated Base-0.5Mn alloy (Fig. 11(c)), although it is still less corroded compared to the Base alloy. In contrast, the T6-treated alloy with 1.0 wt.% Mn addition (Fig. 11(d)) displays serious localized pitting corrosion covering a substantial area, indicating an inferior corrosion resistance compared to the T6-treated Base-0.5Mn alloy. However, the corrosion resistance of the T6-treated Base-1.0Mn alloy is still superior to that of the T6-treated Base alloy. This phenomenon suggests that the addition of Mn is beneficial to inhibiting internal micro-galvanic corrosion and enhancing the corrosion resistance of the T6-treated Al−Si−Mg−Mn alloys.

4 Discussion

As shown in Fig. 12, surface potential maps have been obtained using SKPFM measurements to determine the Volta potential difference (VPD)

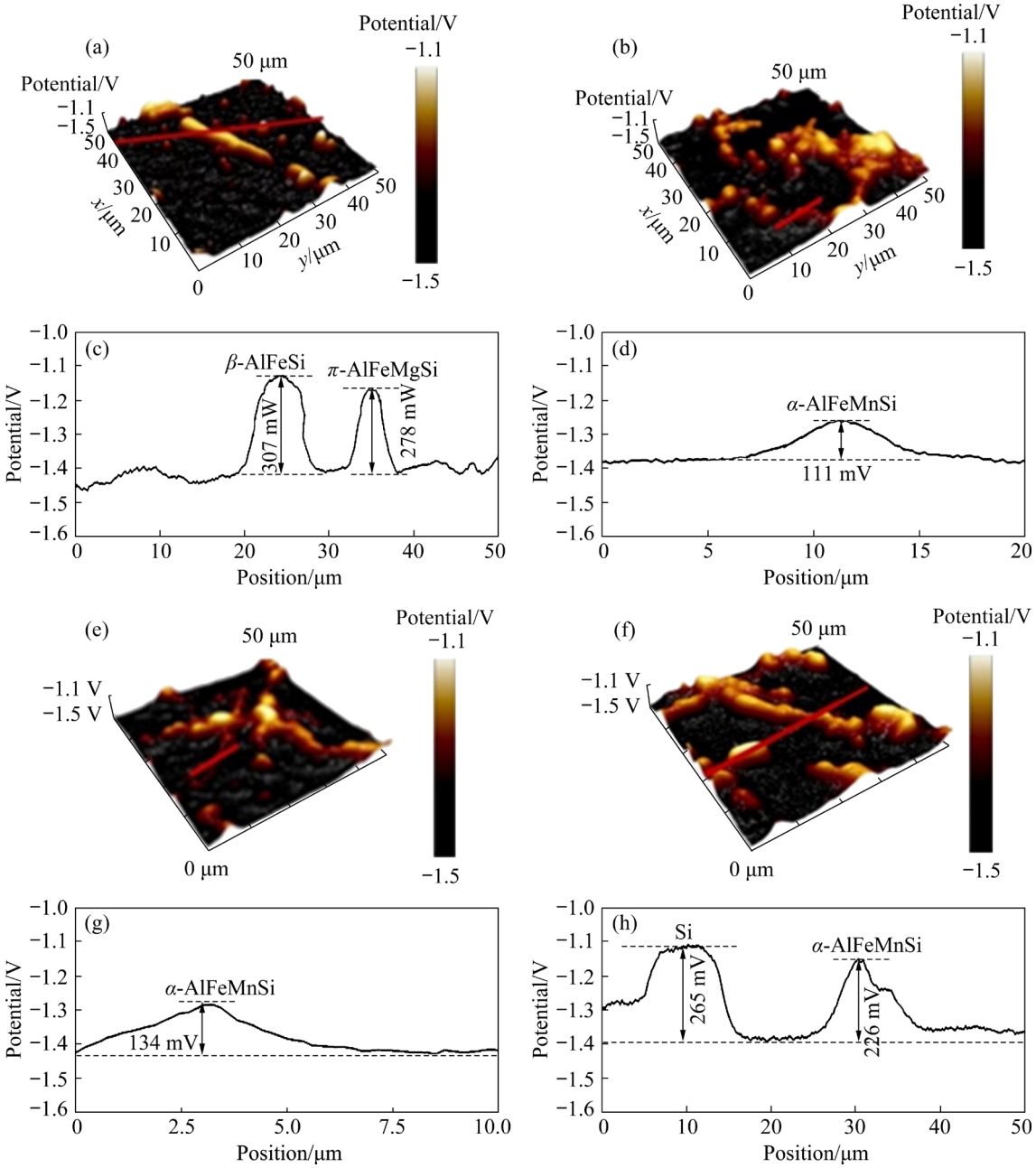

Fig. 12 SKPFM images (a, b, e, f) and corresponding Volta potential profiles (c, d, g, h) along lines in SKPFM images of four T6-treated Al−Si−Mg−*x*Mn alloys: (a, c) Base; (b, d) Base-0.2Mn; (e, g) Base-0.5Mn; (f, h) Base-1.0Mn

between secondary phases and *α*-Al matrix in the T6-treated Al−Si−Mg−*x*Mn alloys, with the VPD distribution along lines in SKPFM images demonstrated in Fig. 12. Secondary phases in the four T6-treated Al−Si−Mg−*x*Mn alloys have larger VPD values in comparison to *α*-Al matrix. This implies that the eutectic Si, *β*-AlFeSi, *π*-AlFeMgSi and *α*-AlFeMnSi phases serve as cathodes, with *α*-Al matrix acting as anode. Specifically, VPD values for *β*-AlFeSi and *π*-AlFeMgSi phases, relative to *α*-Al matrix, are recorded as 307 and 278 mV in the T6-treated Base alloy, respectively (Fig. 12(c)). However, the VPD value for spherical *α*-AlFeMnSi phase in relation to *α*-Al matrix is 111 mV in the T6-treated Base-0.2Mn alloy (Fig. 12(d)), while the VPD value for the eutectic Si phase relative to *α*-Al matrix is 265 mV (Fig. 12(h)). Notably, upon the introduction of 0.5 wt.% Mn and 1.0 wt.% Mn, the VPD values for the needle-like *α*-AlFeMnSi phases exhibit an increase relative to *α*-Al matrix, measuring 134 and 226 mV, respectively (Figs. 12(g, h)).

The *β*-AlFeSi and *π*-AlFeMgSi phases exhibit exceptionally high VPD values relative to *α*-Al

matrix, indicating their higher cathodic activity relative to α-Al matrix, in comparison to the eutectic Si phase relative to α-Al matrix [13]. However, the VPD value of α-AlFeMnSi phase relative to α-Al matrix is smaller than that of eutectic Si phase relative to α-Al matrix, suggesting that α-AlFeMnSi phase has the lowest cathodic activity. Consequently, the presence of α-AlFeMnSi phase on the eutectic Si phase seems to inhibit the cathodic activity of the eutectic Si phase. This transformation of Fe-rich phases due to the addition of Mn reduces the micro-galvanic corrosion effect between secondary phases and α-Al matrix.

During the solution treatment of the four Al−Si−Mg−xMn alloys, the Mg_2Si phase completely dissolves into the α-Al matrix. In the T6-treated Al−Si−Mg−xMn alloys, the Mg_2Si phase primarily exists in the form of precursor β'' phase. Interestingly, despite the presence of Mn, there is no significant influence on the size, distribution, or number density of β'' phase. Therefore, it can be concluded that variations in the corrosion resistance of the T6-treated Al−Si−Mg−xMn alloys are not primarily attributed to the Mg_2Si phase. Based on microstructures and electrochemical results proposed above, we proposed a possible mechanism to explain the effect of Mn on the corrosion behavior of the T6-treated Al−Si−Mg alloys, as shown in Fig. 13. Specifically, Mn affects the type, size and distribution of Fe-rich phases in the T6-treated Al−Si−Mg alloy, and thus affects the corrosion behavior. The VPD values of secondary phases relative to the α-Al matrix are the key factor to determine the micro-galvanic corrosion. The main analysis is as follows: due to the high activity of secondary phases in the alloy, anodic dissolution will occur instead of film forming reaction, resulting in the loss of electrons in the anode α-Al matrix to form Al^{3+}. Finally, Al^{3+} will undergo hydrolysis to produce $Al(OH)_3$ and H^+. The specific reaction steps are shown in Reactions (1) and (2) [46]:

$$Al=Al^{3+}+3e \tag{1}$$

$$xAl^{3+}+yH_2O=Al_x(OH)_y^{3x-y}+yH^+ \tag{2}$$

Therefore, it can be inferred that the higher H^+ formed in the corrosion pit leads to the accelerated dissolution rate of the anode α-Al matrix and the decrease of pH value in corrosion pits. Further, the corrosion behavior can be analyzed according to the change in H^+ concentration in corrosion pits. At the early corrosion stage, the absolute Volta potential values of β-AlFeSi phase and eutectic Si phase are higher than that of the α-Al matrix. Therefore, the β-AlFeSi phase and eutectic Si phase (working as the cathodes) and α-Al matrix (working as the anodes) produce a micro-couple effect to accelerate the corrosion process. In addition, part of the β-AlFeSi phase is distributed on the eutectic Si phase. It makes the cathodic activity of eutectic Si phase higher, resulting in severe corrosion of the α-Al matrix and the formation of corrosion pits (Fig. 13(a)). In the middle stage of corrosion, the corrosion pit around the eutectic Si phase expands and the corrosion pit gathers (Fig. 13(b)). At the later stage of corrosion, due to the continuous dissolution of the anode α-Al matrix, the concentration of H^+ in corrosion pits increases, and the size of corrosion pits further increases (Fig. 13(c)). With 0.2 wt.% Mn added to the Base alloy, the spherical α-AlFeMnSi phase is partially distributed on eutectic Si phase. The VPD value of spherical α-AlFeMnSi phase relative to the α-Al matrix is smaller than that of the eutectic Si relative to the α-Al matrix. Therefore, the spherical α-AlFeMnSi phase inhibits the cathode activity of eutectic Si phase. The corrosion degree of the α-Al matrix is less than that of the Base alloy in the early and middle stages of corrosion, and the size of corrosion pits eventually formed is reduced (Figs. 13(d, e)). At the later stage of corrosion, the H^+ concentration in corrosion pits of Base-0.2Mn alloy is smaller than that of the Base alloy. At the final stage, the size of corrosion pits in the Base-0.2Mn alloy is smaller than that in the Base alloy (Fig. 13(f)). In addition, the spherical α-AlFeMnSi phase is not distributed on eutectic Si phase, which also inhibits the micro-galvanic corrosion in Base-0.2Mn alloy. It weakens the corrosion degree of α-Al matrix, and thus the Base-0.2Mn alloy finally shows an excellent corrosion resistance.

The α-AlFeMnSi phase changes from spherical to needle-like when 0.5 wt.% Mn is added to the Base alloy. The VPD value of needle-like α-AlFeMnSi phase relative to the α-Al matrix is still lower than that of the eutectic Si and β-AlFeSi phases relative to the α-Al matrix. The needle-like α-AlFeMnSi phase distributed on eutectic Si phase still has an inhibitory effect on the cathode activity of eutectic Si phase. The contact area between the

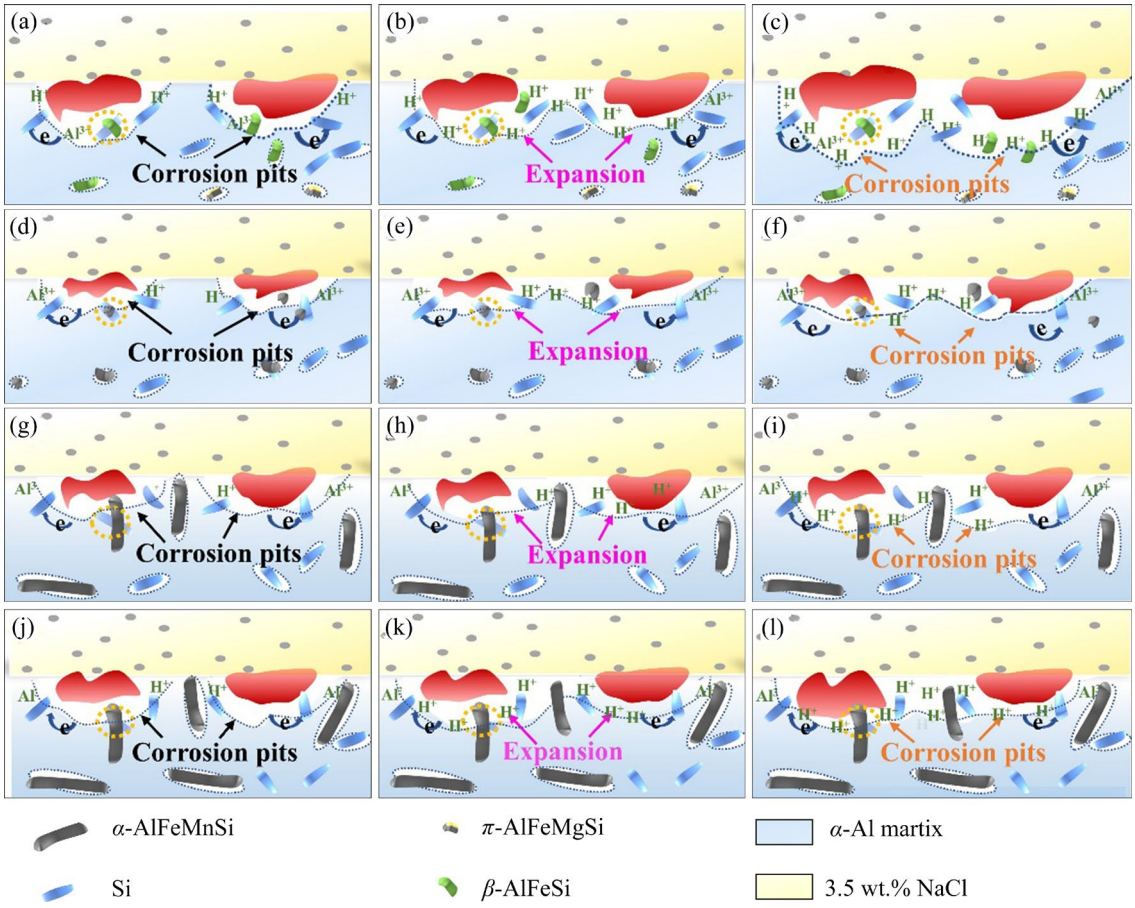

Fig. 13 Schematic illustrations showing initiation and propagation of localized corrosion of four T6-treated Al−Si−Mg−*x*Mn alloys: (a−c) Base; (d−f) Base-0.2Mn; (g−i) Base-0.5Mn; (j−l) Base-1.0Mn

needle-like *α*-AlFeMnSi phase and *α*-Al matrix is larger than that between the spherical *α*-AlFeMnSi phase and *α*-Al matrix. Therefore, the dissolution degree of *α*-Al matrix around the needle-like *α*-AlFeMnSi phase is greater than that around the spherical *α*-AlFeMnSi phase at the early and middle stages of corrosion (Figs. 13(g, h)). At the later stage of corrosion, the H^+ concentration in corrosion pits of base-0.5Mn alloy is higher than that of Base-0.2Mn alloy but still lower than that of Base alloy (Fig. 13(i)).

After adding 1.0 wt.% Mn to the Base alloy, the size and volume fraction of needle-like *α*-AlFeMnSi phase in the Base-1.0Mn alloy continue to increase, resulting in an increase in the contact area between the needle-like *α*-AlFeMnSi phase and *α*-Al matrix. In the early and middle stages of corrosion, the increase in contact area between the needle-like *α*-AlFeMnSi phase and *α*-Al matrix in the Base-1.0Mn alloy leads to the formation of corrosion pits larger than those of the Base-0.5Mn alloy. However, since the VPD value of the needle-like *α*-AlFeMnSi phase relative to *α*-Al matrix is smaller than that of the *β*-AlFeSi phase relative to the *α*-Al matrix, the corrosion degree of the *α*-Al matrix in the Base-1.0Mn alloy is smaller than that of base alloy (Figs. 13(j, k)). At the later stage of corrosion, the concentration of H^+ in corrosion pits of the Base-1.0Mn alloy is greater than that of the Base-0.5Mn alloy, but smaller than that of Base alloy (Fig. 13(l)). Therefore, the decreasing order of corrosion resistance of the four T6-treated Al−Si−Mg−*x*Mn alloys is as follows: Base-0.2Mn > Base-0.5Mn > Base-1.0Mn > Base.

5 Conclusions

(1) When 0.2−1.0 wt.% Mn is added to Al−Si−Mg alloys, the *β*-AlFeSi and *π*-AlFeMgSi phases experience a transformation, converting into the *α*-AlFeMnSi phase. Additionally, Mn does not have a substantial impact on the distribution and size of nano-scale *β″* precipitates in T6-treated Al−Si−Mg alloys.

(2) In the T6-treated Al−Si−Mg alloy, as the Mn content is incrementally increased, the corrosion resistance follows a trend of first rising and then falling. Specifically, the T6-treated Base-0.2Mn alloy demonstrates the most favorable corrosion resistance performance among them.

(3) The VPD value of α-AlFeMnSi phase relative to α-Al matrix is smaller than that of β-AlFeSi relative to α-Al matrix. Accordingly, the formation of α-AlFeMnSi phase can inhibit the micro-galvanic effect. In addition, the spherical or needle-like α-AlFeMnSi phase inhibits the cathode activity of eutectic Si phase, resulting in a decrease in the H^+ concentration in corrosion pits and preventing the expansion of corrosion pits.

(4) The Base-0.2Mn alloy demonstrates a high ultimate tensile strength of ~355 MPa, a yield strength of ~308 MPa, and an elongation of ~8.2%. The enhanced mechanical properties can be attributed to the presence of small-sized spherical α-AlFeMnSi phases.

CRediT authorship contribution statement

Shan-liang XU: Data curation, Writing − Original draft, Writing − Review & editing; **Hai-long JIA:** Conceptualization, Methodology, Validation, Writing − Original draft; **Da-wei WANG:** Methodology, Validation, Visualization, Supervision, Writing − Original draft; **Min ZHA:** Methodology, Data curation, Visualization; **Jia-wang SONG:** Visualization, Data curation; **Xiao-li ZHOU:** Visualization, Data curation; **Pin-kui MA:** Conceptualization, Software, Data curation, Validation, Visualization, Supervision, Writing − Original draft.

Declaration of competing interest

The authors declare that they have no known competing financial interests or personal relationships that could have appeared to influence the work reported in this paper.

Acknowledgments

This work was supported by the National Key Research and Development Program of China (No. 2022YFB3404202), the National Natural Science Foundation of China (No. 52271103), and the Jilin Scientific and Technological Development Program, China (Nos. 20220301026GX, 20210301041GX).

References

[1] LUO Qun, LI Xing-rui, LI Qian, YUAN Ling-yang, PENG Li-ming, PAN Fu-sheng, DING Wen-jiang. Achieving grain refinement of α-Al and Si modification simultaneously by La−B−Sr addition in Al−10Si alloys [J]. Journal of Materials Science & Technology, 2023, 135: 97−110.

[2] CENGIZ S, ABOULFADL H, THUVANDER M. Effect of Ce addition on microstructure, thermal and mechanical properties of Al−Si alloys [J]. Materials Today Communications, 2023, 34: 105518.

[3] PIAO Yi-nan, JIA Hai-long, ZHA Min, MA Pin-kui, GAO Dan, YIN Chao-ran, YANG Zhi-zheng, WANG Hui-yuan. The effect of quenching rates on microstructure and mechanical properties of an Al−Si−Cu−Mg alloy [J]. Materials Characterization, 2023, 196: 112609.

[4] LEE K, KWON Y N, LEE S. Effects of eutectic silicon particles on tensile properties and fracture toughness of A356 aluminum alloys fabricated by low-pressure-casting, casting-forging, and squeeze-casting processes [J]. Journal of Alloys and Compounds, 2008, 461: 532−541.

[5] WANG Rui, WANG Dong-tao, NAGAUMI H, WU Zi-bin, LI Xin-zhong, ZHANG Hai-tao. Understanding the corrosion behavior by passive film evolution in Zn-containing Al−Si−Cu cast alloy [J]. Corrosion Science, 2022, 205: 110468.

[6] MACHADO P A B, QUARESMA J M, GARCIA A, DOS SANTOS C A. Investigation on machinability in turning of as-cast and T6 heat-treated Al−(3,7,12%)Si−0.6%Mg alloys [J]. Journal of Manufacturing Processes, 2022, 75: 514−526.

[7] ZHU B W, ZANELLA C. Hardness and corrosion behaviour of anodised Al−Si produced by rheocasting [J]. Materials & Design, 2019, 173: 107764.

[8] QI Ming-fan, XU Yu-zhao, LI Jing-yuan, KANG Yong-lin, WULABIEKE Z. Microstructure refinement and corrosion resistance improvement mechanisms of a novel Al−Si−Fe−Mg−Cu−Zn alloy prepared by ultrasonic vibration-assisted rheological die-casting process [J]. Corrosion Science, 2021, 180: 109180.

[9] KRUEHONG C, EL-MAHDY G A, NISHIKATA A, TSURU T. Influence of second phases on the electrochemical behavior of hot dipped Al−Mg−Si coated steel [J]. Corrosion Science, 2010, 52: 2379−2386.

[10] CHEN Ming-yang, ZHENG, Xu HE Ke-zhun, LIU Sheng-dan, ZHANG Yong. Local corrosion mechanism of an Al−Zn−Mg−Cu alloy in oxygenated chloride solution: Cathode activity of quenching-induced η precipitates [J]. Corrosion Science, 2021, 191: 109743.

[11] XU X, HAO M, CHEN J, HE W, LI G, LI K, JIAO C, ZHONG X L, MOORE K L, BURNETT T L, ZHOU X. Role of constituent intermetallic phases and precipitates in initiation and propagation of intergranular corrosion of an Al−Li−Cu−Mg alloy [J]. Corrosion Science, 2022, 201: 110294.

[12] FARAHANY S, OURDJINI A, BAKHSHESHI-RAD H R. Microstructure, mechanical properties and corrosion behavior of Al−Si−Cu−Zn−X (X=Bi, Sb, Sr) die cast alloy [J]. Transactions of Nonferrous Metals Society of China, 2016, 26: 28−38.

[13] ARRABAL M B, PARDO A, MOHEDANO M, MATYKINA E, RODRÍGUEZ I. Pitting corrosion of rheocast A356 aluminium alloy in 3.5 wt.% NaCl solution [J]. Corrosion Science, 2013, 73: 342−355.

[14] HAI Li, ZHAO Pei-pei, WANG Zhi-xiu, MAO Qing-zhong, FANG Bi-jun, SONG Ren-guo, ZHENG Zi-qiao. The intergranular corrosion susceptibility of a heavily overaged Al−Mg−Si−Cu alloy [J]. Corrosion Science, 2016, 107: 113−122.

[15] ZHENG Yan, XIAO Wen-long, GE Su-jing, ZHAO Wei-tao, HANADA S, MA Chao-li. Effects of Cu content and Cu/Mg ratio on the microstructure and mechanical properties of Al−Si−Cu−Mg alloys [J]. Journal of Alloys and Compounds, 2015, 649: 291−296.

[16] ARTHANARI S, JANG J C, SHIN K S. Corrosion performance of high pressure die-cast Al−Si−Mg−Zn alloys in 3.5 wt.% NaCl solution [J]. Journal of Alloys and Compounds, 2019, 783: 494−502.

[17] SHI Hong-wei, HAN En-hou, LIU Fu-chun, WEI Tao, ZHU Zheng-wang, XU Dao-kui. Study of corrosion inhibition of coupled Al_2Cu−Al and Al_3Fe−Al by cerium cinnamate using scanning vibrating electrode technique and scanning ion-selective electrode technique [J]. Corrosion Science, 2015, 98: 150−162.

[18] KAYANI S H, HA H Y, KIM B J, CHO Y H, SON H W, LEE J M. Impact of intermetallic phases on the localised pitting corrosion and high-temperature tensile strength of Al−Si−Mg−Cu−Ni alloys [J]. Corrosion Science, 2024, 233: 112064.

[19] KAYANI S H, HA H Y, CHO Y H, SON H W, LEE J M. Dislocation-assisted localised pitting corrosion behaviour of Al−Si−Mg−Cu−Mn alloy [J]. Corrosion Science, 2023, 221: 111372.

[20] ZOU Yong-cheng, YAN Hong, YU Bao-biao, HU Zhi. Effect of rare earth Yb on microstructure and corrosion resistance of ADC12 aluminum alloy [J]. Intermetallics, 2019, 110: 106487.

[21] ZHENG Qiu-ju, WU Jing, JIANG Hong-xiang, ZHANG Li-li, ZHAO Jiu-zhou, HE Jie. Effect of micro-alloying element La on corrosion behavior of Al−Mg−Si alloys [J]. Corrosion Science, 2021, 179: 109113.

[22] GENG Run, JIA Si-qi, QIU Feng, ZHAO Qing-long, JIANG Qi-chuan. Effects of nanosized TiC and TiB_2 particles on the corrosion behavior of Al−Mg−Si alloy [J]. Corrosion Science, 2020, 167: 108479.

[23] NIU Guo-dong, WANG Jian-feng, YE Jin-wen, MAO Jian. Enhancing Fe content tolerance in A356 alloys for achieving low carbon footprint aluminum structure castings [J]. Journal of Materials Science & Technology, 2023, 161: 180−191.

[24] WANG Yu, DENG Yun-lai, DAI Qing-song, JIANG Ke-da, CHEN Ji-qiang, GUO Xiao-bin. Microstructures and strengthening mechanisms of high Fe containing Al−Mg−Si−Mn−Fe alloys with Mg, Si and Mn modified [J]. Materials Science and Engineering: A, 2021, 803: 140477.

[25] CHOMSAENG N, HARUTA M, CHAIRUANGSRI T, KURATA H, ISODA S, SHIOJIRI M. HRTEM and ADF-STEM of precipitates at peak-ageing in cast A356 aluminium alloy [J]. Journal of Alloys and Compounds, 2010, 496: 478−487.

[26] CHEN Ying, YUAN Xu, DONG Jia-hui, JIN Shen-bao, SHA Gang, YANG Yi-hang, ZHANG Hou-an, WANG Chuan-ting, GAO Nong, STARINK M J. The nanoscale mechanisms of strengthening and ductility enhancement in an Al−Mg−Si−Mn alloy on processing by high-pressure torsion [J]. Materials Characterization, 2023, 203: 113145.

[27] WANG Bing, WANG Jun-sheng, LIU Xin-xiu, LI Quan, LIU Xiao-guang. Uncovering the effects of neutralizing elements (Co, Mn and Cr) on the Fe-rich intermetallic formation in Al−Si−Cu alloys [J]. Materials Science and Engineering: A, 2022, 858: 144090.

[28] LIU Xu, JIA Hai-long, WANG Cheng, WU Xian, ZHA Min, WANG Hui-yuan. Enhancing mechanical properties of twin-roll cast Al−Mg−Si−Fe alloys by regulating Fe-bearing phases and macro-segregation [J]. Materials Science and Engineering: A, 2022, 831: 142256.

[29] HWANG J Y, DOTY H W, KAUFMAN M J. The effects of Mn additions on the microstructure and mechanical properties of Al−Si−Cu casting alloys [J]. Materials Science and Engineering: A, 2008, 488: 496−504.

[30] NIU G D, WANG J, LI J P, YE J W, MA J. Characterization of in-situ reinforced $(Al,Si)_3(Ti,Ce)$ precipitates in T6 treated A356−0.3wt.%Ce−1.5vol.%TiCN composite and its effects on mechanical properties [J]. Materials Characterization, 2022, 185: 111756.

[31] HE Sheng-yang, DU Jing-hong, JI Quan-xin, QIN Chao-qian, CHEN Jia-xing, LV Jia-hao, YANG Jia-rui. Effect of Zr content on microstructure and tensile properties of cast and T6 heat-treated A356-0.3Yb alloy [J]. Materials Research Express, 2023, 10: 066503.

[32] ASGHAR G, PENG Li-ming, FU Peng-huai, YUAN Ling-yang, LIU Yue. Role of Mg_2Si precipitates size in determining the ductility of A357 cast alloy [J]. Materials & Design, 2020, 186: 108280.

[33] WEI Qi, XU Hong, BAI Xiao-yu, LIAN Peng, WANG Yu, MAO Hong-kui, WANG Cong. Effect of Sc on microstructure and properties of A357 alloy under different casting conditions [J]. Journal of Materials Research and Technology, 2022, 20: 2051−2059.

[34] GUO Rui, HE Jian-gang, LI Feng-guang, SHI Qiu-yue, ZENG Da-xin. Effects of Zn content on the microstructure and properties of Al−12.5Si−*x*Zn−2Cu−Mg alloy [J]. International Journal of Metalcasting, 2023, 17: 2298−2307.

[35] CESCHINI L, MESSIERI S, MORRI A, SEIFEDDINE S, TOSCHI S, ZAMANI M. Effect of Cu addition on overaging behaviour, room and high temperature tensile and fatigue properties of A357 alloy [J]. Transactions of Nonferrous Metals Society of China, 2020, 30: 2861−2878.

[36] PRAMOD S L, RAVIKIRANA A K, PRASADARAO A K, MURTY B S, BAKSHI R. Microstructure and mechanical properties of as-cast and T6 treated Sc modified A356-5TiB_2 in-situ composite [J]. Materials Science and Engineering: A, 2019, 739: 383−394.

[37] WANG Tong-min, ZHAO Yu-fei, CHEN Zong-ning, ZHENG Yuan-ping, KANG Hui-jun. Combining effects of TiB_2 and La on the aging behavior of A356 alloy [J]. Materials Science and Engineering: A, 2015, 644: 425−430.

[38] YIN Si-qi, DUAN Wen-chao, LIU Wen-hong, WU Liang, BAO Jia-xin, YU Jia-min, LI Liang, ZHAO Zhong, CUI Jian-zhong, ZHANG Zhi-qiang. Improving the corrosion resistance of MgZn1.2Gd*x*Zr0.18 (*x*=0, 0.8, 1.4, 2.0) alloys via Gd additions [J]. Corrosion Science, 2020, 177: 108962.

[39] WANG Bing-yu, LI Mei-xuan, LI Yi-jia, WANG Yu-fei,

GAO Yi-peng, WANG Hui-yuan. Effect of Al/Mn ratio on corrosion behavior of lean Mg−Zn−Ca−Al−Mn alloy processed by twin-roll casting [J]. Corrosion Science, 2023, 212: 110938.

[40] LI Yi-jia, LI Mei-xuan, HUA Zhen-ming, WANG Bing-yu, GAO Yi-peng, WANG Hui-yuan. Role of alloyed Al on the microstructure and corrosion behavior of as-cast dilute Mg−2Zn−*x*Al−0.5Ca alloys [J]. Corrosion Science, 2023, 211: 110861.

[41] MA Yu-kun, LIU Ya-nan, WANG Ming-xing. Microstructures and corrosion resistances of hypoeutectic Al−6.5Si−0.45 Mg casting alloy with addition of Sc and Zr [J]. Materials Chemistry and Physics, 2022, 276: 125321.

[42] SONG Ying-wei, HAN En-hou, SHAN Da-yong, CHANG Dong, YOU Bong-sun. The effect of Zn concentration on the corrosion behavior of Mg−*x*Zn alloys [J]. Corrosion Science, 2012, 65: 322−330.

[43] CHOI H Y, KIM W J. The improvement of corrosion resistance of AZ91 magnesium alloy through development of dense and tight network structure of Al-rich α phase by addition of a trace amount of Ti [J]. Journal of Alloys and Compounds, 2017, 696: 736−745.

[44] ZHANG Kai, WANG Cheng, LIU Shi, GUAN Kai, ZHANG Lin-yang, WANG Hui-yuan. New insights on corrosion behavior of aging precipitates in dilute Mg−Al−Ca alloy by experiments and first-principles calculations [J]. Corrosion Science, 2023, 220: 111254.

[45] LIU Cheng-long, XIN Yun-chang, TANG Guo-yi, CHU P K. Influence of heat treatment on degradation behavior of bio-degradable die-cast AZ63 magnesium alloy in simulated body fluid [J]. Materials Science and Engineering: A, 2007, 456: 350−357.

[46] SZUNERITS S, WALT D R. Aluminum surface corrosion and the mechanism of inhibitors using pH and metal ion selective imaging fiber bundles [J]. Analytical Chemistry, 2002, 74: 886−894.

Mn 添加对 T6 态 Al−Si−Mg 合金显微组织、力学性能和腐蚀行为的影响

徐善良[1]，贾海龙[1,2]，王大为[1]，查 敏[1,2]，宋家旺[1]，周晓丽[1]，马品奎[1]

1. 吉林大学 材料科学与工程学院 教育部汽车材料重点实验室，长春 130025；
2. 吉林大学 未来科学国际合作联合实验室，长春 130012

摘 要：研究了 Mn 添加对 T6 态 Al−Si−Mg−*x*Mn (*x*=0.2%−1.0%，质量分数)合金显微组织、力学性能及在 3.5% NaCl (质量分数)溶液中腐蚀行为的影响。结果显示，添加 0.2% Mn (质量分数)可通过促进 α-AlFeMnSi 相的形成，提高 T6 态 Al−Si−Mg 合金的耐蚀性，该相与共晶 Si、β-AlFeSi 和 π-AlFeMgSi 相相比，具有更小的绝对伏特电势值。然而，T6 态 Al−Si−Mg 合金中添加 0.5% Mn (质量分数)和 1.0% Mn (质量分数)增加了 α-AlFeMnSi 相的尺寸，降低了 T6 态 Al−Si−Mg 合金的性能。因此，最佳 Mn 含量为 0.2% (质量分数)，为改善 Al−Si−Mg 合金的力学性能和耐蚀性提供了一种协同增强的新方法。

关键词：Al−Si−Mg−*x*Mn 合金；第二相；绝对伏特电势；显微组织；力学性能；耐蚀性

(Edited by Wei-ping CHEN)